Eur. Phys. J. D **18**, 179–190 (2002)
DOI: 10.1140/epjd/e20020022

THE EUROPEAN PHYSICAL JOURNAL D
EDP Sciences

Triggered single photons and entangled photons from a quantum dot microcavity

M. Pelton[1,a], C. Santori[1], G.S. Solomon[1,2], O. Benson[3], and Y. Yamamoto[1,4]

[1] Quantum Entanglement Project, ICORP, JST, E. L. Ginzton Laboratory, Stanford University, Stanford CA-94305, USA
[2] Solid-State Photonics Laboratory, Stanford University, Stanford CA-94305, USA
[3] Physics Department, University of Konstanz, Universitätsstrasse 10, 78464 Konstanz, Germany
[4] NTT Basic Research Laboratories, Atsugishi, Kanagawa, Japan

Received 8 July 2001 and Received in final form 25 August 2001

Abstract. Current quantum cryptography systems are limited by the attenuated coherent pulses they use as light sources: a security loophole is opened up by the possibility of multiple-photon pulses. By replacing the source with a single-photon emitter, transmission rates of secure information can be improved. We have investigated the use of single self-assembled InAs/GaAs quantum dots as such single-photon sources, and have seen a tenfold reduction in the multi-photon probability as compared to Poissonian pulses. An extension of our experiment should also allow for the generation of triggered, polarization-entangled photon pairs. The utility of these light sources is currently limited by the low efficiency with which photons are collected. However, by fabricating an optical microcavity containing a single quantum dot, the spontaneous emission rate into a single mode can be enhanced. Using this method, we have seen 78% coupling of single-dot radiation into a single cavity resonance. The enhanced spontaneous decay should also allow for higher photon pulse rates, up to about 3 GHz.

PACS. 78.67.Hc Quantum dots – 42.50.Dv Nonclassical field states; squeezed, antibunched, and sub-Poissonian states; operational definitions of the phase of the field; phase measurements – 73.21.-b Electron states and collective excitations in multilayers, quantum wells, mesoscopic, and nanoscale systems

1 Introduction

Quantum cryptography has emerged as a significant field of study over the last fifteen years, because it offers the promise of private communication whose security is assured by the laws of physics. Most implementations of quantum cryptography so far have used a protocol introduced by Bennet and Brassard, generally known as BB84, which uses four different states of a quantum system [1]. For example, the message can be encoded on the polarization state of single photons, with a random choice between two non-orthogonal polarization bases when the photons are sent and received. Since an eavesdropper does not know what bases have been chosen, any measurement she makes will impose a detectable back-action on the states of the transmitted photons. Using error correction and privacy amplification, the communicating parties can distill the transmitted message into a secure key, about which the eavesdropper knows arbitrarily little.

However, sources of single photons have not been generally available. Experimental implementations of BB84 have used pulses from lasers or light-emitting diodes, attenuated to the point where the average photon number per pulse is significantly less than one [2]. However, the number of photons in these pulses is described by Poissonian statistics, so that there is always a possibility of more than one photon being sent in a given pulse. Such pulses are vulnerable to a photon-splitting attack, where the eavesdropper removes one photon from the pulse, leaving the remaining photons undisturbed [3]. This increases the required privacy amplification, reducing the length of the secure string. In other words, for communication over a given channel, the number of secure bits per pulse will be greater for a true single-photon source than for Poissonian light [4].

Any real light source will have a non-zero probability of producing more than one photon in a given pulse. However, as the probability of multi-photon pulses is reduced, the rate of secure communication will increase. A pulse stream with reduced multi-photon probability compared to the Poissonian case is said to be *antibunched*, and can be described only quantum mechanically. Mathematically, such non-classical photon statistics can be described using

[a] e-mail: pelton@stanford.edu

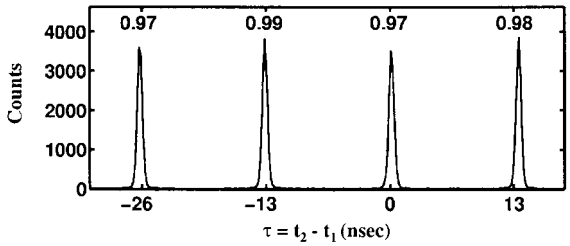

Fig. 1. Measured photon-photon correlation function for pulses from a mode-locked Ti:sapphire laser with a 13 ns repetition period. The numbers above the peaks are the normalized areas.

the photon correlation function $g^{(2)}(\tau)$, defined as follows:

$$g^{(2)}(\tau) = \frac{\langle \hat{a}^\dagger(t)\hat{a}^\dagger(t+\tau)\hat{a}(t+\tau)\hat{a}(t)\rangle}{\langle \hat{a}^\dagger\hat{a}\rangle^2}\,, \qquad (1)$$

where $\hat{a}^\dagger$ and $\hat{a}$ are the photon creation and annihilation operators, respectively. A pulsed source with Poissonian statistics will have a $g^{(2)}(\tau)$ function consisting of a series of peaks with unit area, when normalized by the pulse repetition period. This can be seen in Figure 1, which shows a measured photon correlation function for attenuated pulses from a mode-locked laser. (See below for an explanation of the measurement method.) This reflects the fact that the probability of detecting a photon in a given pulse is independent of whether a photon has already been detected. For an ideal single-photon source, the central peak at $\tau = 0$ is absent, indicating that, once a single photon has been detected in a pulse, another one will never be detected. An antibunched source will have a zero-delay peak with an area between zero and one. This area gives an upper bound on the probability $P(n_j \geq 2)$ that two or more photons are present in the same pulse:

$$2P(n_j \geq 2)/\langle n\rangle^2 \leq \frac{1}{T}\int_{-\epsilon}^{\epsilon} g^{(2)}(\tau)\mathrm{d}\tau \qquad (2)$$

where $\langle n\rangle$ is the mean photon number per pulse, T is the pulse repetition period, and the interval $[-\epsilon, \epsilon]$ contains the entire central peak. In a quantum communication system, this interval would be the time window for gated detection of the signal pulse.

Recently, several systems have been investigated for production of single photons. Continuous streams of antibunched photons have been produced using single atoms and ions [5], single molecules [6], and color centers in diamond crystals [7]. Pulses of antibunched photons have been produced by exciting single molecules using a laser pulse [8] or using adiabatic following [9], or by controlled injection of single carriers into a quantum well [10]. Progress has also been made towards a single-photon source using single atoms strongly coupled to an optical cavity [11]. The common factor in all of these sources is that the photons are produced by a single emitter, be it a molecule, atom, ion, color center, or an electron-hole pair in a quantum-well. The essential principle of operation is always the same: a single emitter can only emit one photon at a time.

Excitons in quantum dots are also promising as single-photon sources, since they too behave as single emitters. It has been shown that the fluorescence from a single quantum dot exhibits antibunching [12]. We have achieved triggered generation of antibunched photons from a single quantum dot by exciting with a pulsed laser and spectrally filtering the emission [13]. The normalized area of the $g^{(2)}(0)$ peak can be as low as 0.113. This system for generating single photons, which has also been reported by other groups [14], is stable over long periods of time and is compatible with mature semiconductor technologies. This allows for the possibility of injecting carriers into the dot electrically instead of optically, producing arrays of sources, and integrating into larger structures.

For example, the quantum dot can be fabricated within a microscopic optical cavity in order to increase the efficiency of the single-photon source. If an emitter is located inside a cavity with a small mode volume and a high finesse, its spontaneous-emission properties are changed. For example, if the emitter is on resonance with a cavity mode, the spontaneous emission rate into this mode is enhanced [15]. This so-called Purcell effect has been seen in atoms for over fifteen years [16]. More recently, ensembles of quantum dots have been coupled to three-dimensionally confined modes in semiconductor microcavities, and changes in their spontaneous-emission lifetimes have been seen [17]. We have succeeded in enhancing the spontaneous emission rate from a single quantum dot into a single mode of an optical microcavity [18]. Because of the enhanced coupling into a single cavity mode, the spontaneous emission becomes directional. A large fraction of the photons can thus be coupled into downstream optical components.

Finally, the single quantum dot can serve as a source of other non-classical radiation states. For example, there may be the possibility to create triggered pairs of polarization-entangled photons [19]. These photon pairs could be used in quantum communication systems that use different schemes, such as the Ekert protocol [20].

2 Single indium arsenide/gallium arsenide quantum dots

Semiconductor quantum dots are small regions of a low-bandgap semiconductor inside a crystal of a larger-bandgap semiconductor. The bandgap difference acts as a potential barrier for carriers, confining them inside the dot. Quantum dots are small enough that the carriers form standing waves inside the confinement region, and can only occupy discrete energy levels. Interest in quantum dots was stimulated by the discovery that structures with the required characteristics form spontaneously during epitaxial growth of lattice-mismatched materials [21]. For example, when InAs is deposited on GaAs, a strained planar layer, known as a wetting layer, initially forms. The strain energy that builds up in this layer is eventually partially relieved by the formation of nanometer-scale

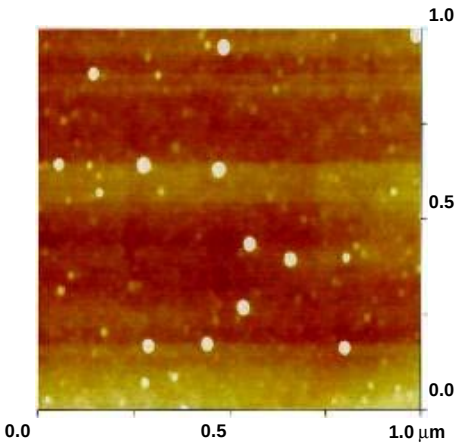

Fig. 2. Atomic-force-microscope image of sparse self-assembled InAs quantum dots grown on GaAs.

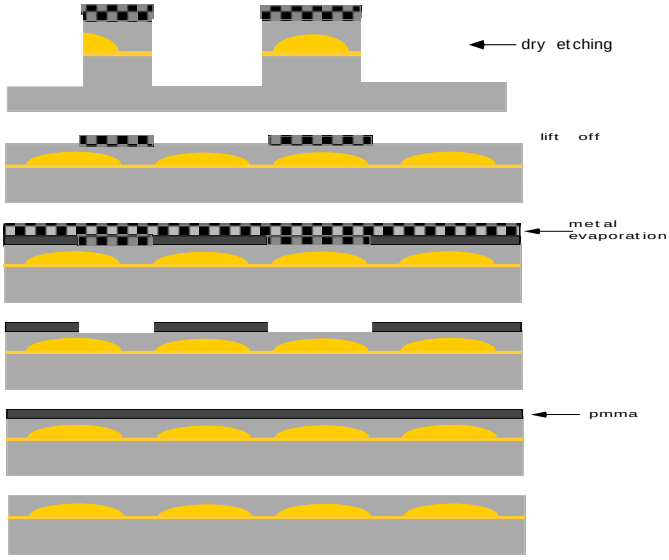

Fig. 3. Schematic illustration of the process used to fabricate microposts in a sample containing InAs/GaAs quantum dots. The process steps are shown sequentially from bottom to top. Starting with an MBE-grown sample, an electron-beam-sensitive resist is spun on top. Electron-beam lithography is used to draw mall holes in the resist, and metal is then evaporated on top. The resist is dissolved in a solvent, lifting off the portions of metal above it. A dry etching process is then used to remove the parts of the sample not protected by the metal mask.

islands on the surface. The islands form without defects, and can subsequently be covered with a capping layer of GaAs. Transitions between confined conduction-band and valence-band states involve the absorption or emission of photons at near-optical frequencies. These structures have been extensively studied, both for their intrinsic physical interest and for possible applications in optoelectronic devices [22].

We grew InAs/GaAs quantum dots by molecular beam epitaxy (MBE). In MBE, high-quality heterostructures are obtained by epitaxial deposition in ultra-high vacuum [23]. Elemental sources (In, Ga, and As) are heated to produce molecular beams, which impinge on a heated substrate. Atomic layer-by-layer deposition is achieved by using low molecular fluxes, and shutters in front of the sources are used to control growth time. By controlling the growth rate, the substrate temperature, the ratio of As to In impinging on the surface, and the amount of material deposited, it is possible to control the size and density of the quantum dots [24]. The samples used in our experiments were grown under conditions that give relatively sparse dots, with a surface density of 11–75 $\mu\mathrm{m}^{-2}$. Figure 2 shows an atomic-force microscope image of dots similar to those used in our experiments, except for the absence of a GaAs capping layer.

Single dots are isolated by etching mesas in the MBE-grown sample. The mesas are fabricated by electron-beam lithography and dry etching [25]. Figure 3 outlines the steps used. An electron-beam resist is spin-coated onto the surface of the sample. In our case, we use a two-layer resist consisting of poly-methyl methacrylate (PMMA) of different molecular weights. The sample is then introduced into a scanning electron microscope. An electron beam is moved across the surface in order to expose a pattern of circles in the resist. The exposed sample is developed in a solvent mixture, which dissolves away the portions of the resist that were exposed to the electron beam. A thin layer of gold is then deposited on the surface using electron-beam evaporation. Next, the remaining PMMA is dissolved in acetone, which removes both the resist and the gold above it, leaving behind a pattern (etch mask) of metal circles. The sample is then introduced into an electron-cyclotron resonance plasma etcher. This etcher is a vacuum chamber which contains a mixture of Ar, Cl_2, and BCl_3 gases at low pressure. Microwaves at the electron cyclotron frequency ionize the gas, and permanent magnets confine the resulting plasma. A radio-frequency field is applied to the sample, creating an effective bias in the plasma above the surface. Ions are thereby accelerated towards the sample, where they react with and remove GaAs and InAs. This etch process is highly directional, producing small mesas below the metal circles. The mesas used for isolating single dots are about 120 nm tall and 200 nm wide, and are spaced 50 μm apart.

The single quantum dots are probed by photoluminescence (PL). Figure 4 shows the experimental apparatus used. The sample is held at a temperature of 4 K in a continuous-flow liquid-helium cryostat, and is held close to the cryostat window. Light from a tunable, mode-locked Ti:sapphire laser is focussed onto a post from a steep angle, down to an 18 μm effective spot diameter. The laser can be tuned to have a photon energy larger than the GaAs bandgap. In this case, a large number of electron-hole pairs are created in the GaAs matrix surrounding the quantum dot. The carriers diffuse towards the dot, where they are rapidly trapped, and quickly relax to the lowest confined states [26]. Alternatively, the laser energy can be tuned so that it is equal to the transition energy between higher-lying confined states in the dot. This eliminates the

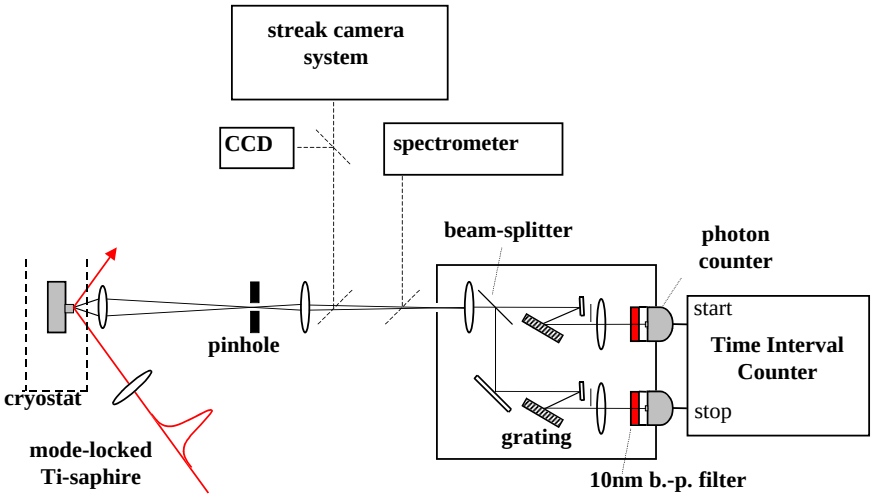

Fig. 4. Schematic of the setup used to measure luminescence from single quantum dots.

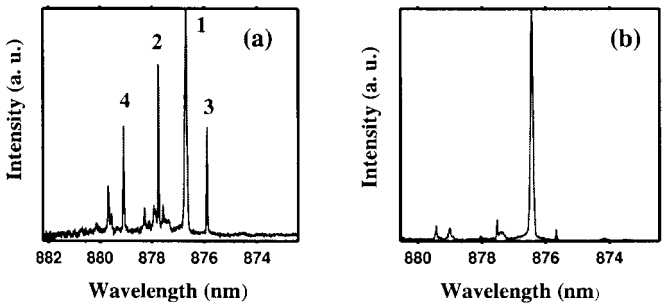

Fig. 5. Photoluminescence spectra from a single InAs/GaAs self-assembled quantum dot. For (a), the pump laser had an energy above the GaAs bandgap. For (b), the pump energy was resonant with a higher-order transition in the dot, so that excitons are created only in the dot.

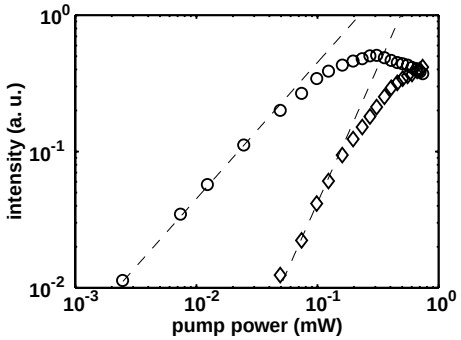

Fig. 6. Luminescence intensity from a single quantum dot as a function of incident above-band pump power. Circles represent the integrated intensity under the single-exciton line, while diamonds represent the biexciton line.

necessity for carriers to diffuse to the dot and be captured into the confined states, and ensures charge neutrality in the dot.

Light emitted from the dot is collected by an aspheric lens that has a numerical aperture of 0.5, and is focused onto a pinhole that isolates an effective 5 μm region of the sample. The light is then sent to a charge-coupled device (CCD) camera, a spectrometer, a streak camera, or a Hanbury Brown-Twiss configuration (described below) for measuring the photon correlation function. The CCD camera allows us to monitor the sample through the collection lens, making alignment possible. The spectrometer has a resolution of 0.05 nm and a cooled CCD array on the output. Figure 5 shows PL spectra from the quantum dot used to generate single photons. With continuous-wave (CW) excitation above the GaAs bandgap, the emission spectrum displays several lines [27]. We believe that these lines all come from a single dot, because other mesas show nearly identical emission patterns (peak heights, spacings and widths), except for an overall wavelength shift, suggesting that this pattern is not random. When the laser is tuned to an absorption resonance at 857.5 nm, thus creating excitons directly inside the dot, emission peaks 3 and 4 almost disappear. We therefore believe that they represent emission from other charge states of the dot [28]. We identify peak 1 as ground-state emission after the capture of a single exciton, and peak 2 as "biexcitonic" emission after the capture of two excitons. A biexcitonic energy shift of 1.7 meV is seen, due to electrostatic interactions among carriers.

Assignment of the different peaks is supported by the dependence of the emission line intensities on pump power, as shown in Figure 6. In this case, we are using CW excitation above the GaAs bandgap. We can see linear growth of peak 1 and quadratic growth of peak 2 in the weak-pump limit, as expected for excitons and biexcitons, respectively. Further support for the peak identification comes from time-dependent spectra, as collected by the streak camera [29]. This now requires pulsed excitation, again above the GaAs bandgap. The camera produced two-dimensional images of intensity *vs.* wavelength and time after exciting with a laser pulse. Integration times

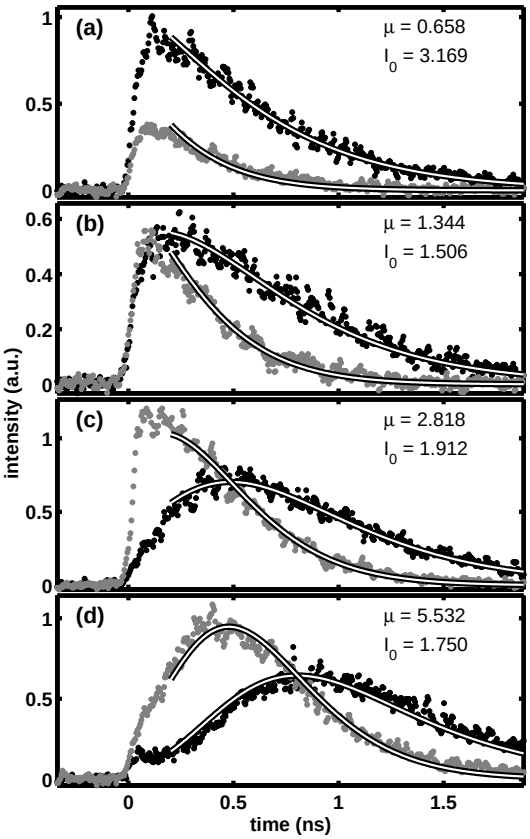

Fig. 7. Time-dependence luminescence intensities of the single-exciton line 1 (black) and the biexciton line 2 (gray) after pulsed excitation above the GaAs bandgap. Hollow lines show model fit results, with the parameter values for the fits shown in the figures. The pump powers are (a) 27 μW, (b) 54 μW, (c) 108 μW, and (d) 432 μW.

were about 5 minutes. Time resolution as determined by the spectrometer is about 25 ps. The images were corrected for background counts, non-uniform sensitivity, and a small number of cosmic ray events. By integrating intensity within frequency windows corresponding to the peaks shown in Figure 5, time-dependent intensities are obtained for the different lines. The results are shown in Figure 7 for different pump powers.

Under weak excitation, the single-exciton line (line 1) appears quickly after the excitation pulse, and then decays exponentially. This decay time has been measured independently under resonant excitation to be 0.47 ns. Under higher excitation power, however, line 1 reaches its maximum only after a long delay. Most of the emission immediately after the excitation pulse now comes from line 2. Since the laser pulse now initially creates several exciton-hole pairs on average, some time is required before the population of the dot reduces to one electron-hole pair, and only then can the one-exciton emission occur.

A simple quantitative model can describe these results. Photons from the laser excitation pulse are assumed to be absorbed independently from each other, so that the number of created excitons follows a Poisson distribution. We also assume that excitons decay independently from each other, giving a decay rate proportional to the exciton number. That is, we assume perfect selection rules, so that each electron can recombine with only one particular hole. These assumptions result in a Poisson-distributed exciton population for all times after the excitation pulse, with an exponentially decaying mean:

$$P_n(t) = (\mu \mathrm{e}^{-\gamma t})^n \exp(-\mu \mathrm{e}^{-\gamma t})/n!\,, \tag{3}$$

where $P_n(t)$ is the probability that n excitons exist in the dot at time t, μ is the mean number of excitons at time zero, and γ is the radiative decay rate. Given that the intensity $I_n(t)$ of the n-exciton line should be proportional to its radiative decay rate, we obtain

$$I_n(t) = I_0 n P_n(t)\,, \tag{4}$$

where I_0 is a constant proportional to the efficiency with which the emitted photons are collected and detected.

Fitted curves from this model are shown as solid lines in Figure 7. The same μ is used for all emission lines at given excitation power. I_0 varies between streak camera images, due to sample drift and streak-camera gain drift. The fitting parameters μ and I_0 were determined by minimizing the total sum-of-squares error between the model and both lines for a given streak camera image. The model is seen to provide an excellent fit to the data, supporting the assignment of single-exciton and biexciton peaks.

To test our assumptions, we considered another model, where the selection rules are absent. This means that each electron may recombine with equal probability with each hole, so that the decay rate is quadratic in the exciton number. With this model, it was impossible to obtain a good fit to the observed time-dependent spectra, regardless of the values of the fitting parameters. We point out two important features of the data that this model cannot reproduce. First, the decay rate of the two-exciton state long after the excitation pulse is experimentally observed to be very close to twice the one-exciton decay rate, while the model without selection rules would predict it to be four times larger. Secondly, for large initial exciton populations ($\mu \to \infty$), the one-exciton probability in this model reaches its maximum at $0.906/\gamma = 0.43$ ns. This is only half as long as the delay seen in Figure 7d.

3 Generation of non-classical light

Since peak 1 corresponds to emission from a quantum dot containing a single exciton, there should be only one photon emitted at this energy for each excitation laser pulse, regardless of the number of electron-hole pairs originally created inside the dot [30]. Spectral filtering was used to select this last photon, resulting in only one photon per pulse. For this measurement, the quantum dot was excited with a pump energy resonant with a higher-lying transition in the dot, below the GaAs bandgap. As shown in Figure 4, a monochrometer-type configuration was used to define a 2 nm-wide measurement bandwidth, with the

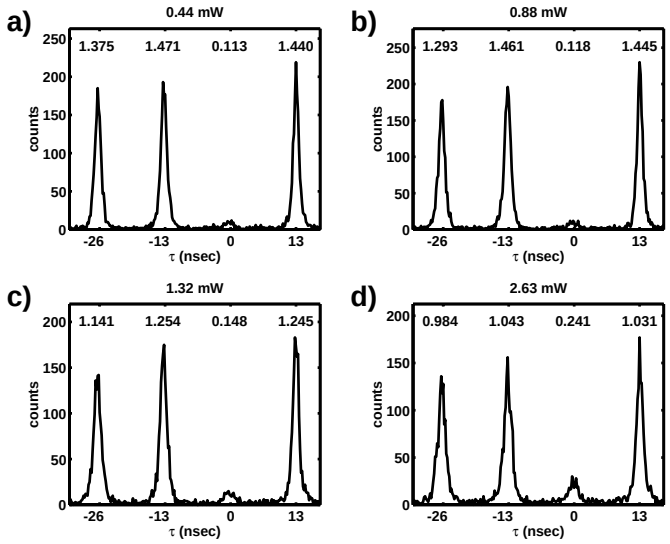

Fig. 8. Photon-photon correlation functions for emission from a single InAs/GaAs quantum dot under pulsed, resonant excitation by a Ti:sapphire laser. (a) through (d) represent different pump powers, as indicated. The plots show unprocessed histograms of time intervals as measured by the Hanbury Brown and Twiss-type apparatus. The numbers above the peaks represent the normalized peak areas, calculated using a 0.56 ns-wide integration window.

center wavelength determined by the detector position. Additional rejection of unwanted light (scattered pump light and stray room light) was achieved with a 10 nm bandpass filter attached to each detector.

The Hanbury Brown and Twiss-type configuration was used to measure the photon correlation function. A beamsplitter sends photons towards one of two single-photon detectors. The detectors are EG&G "SPCM" avalanche photodiodes, which have efficiencies of 40% at 877 nm and 0.2 mm-wide active areas. The electronic pulses from the photon counters were used as start (t_1) and stop (t_2) signals for a time-interval counter, which recorded a histogram of delays $\tau = t_2 - t_1$. Normalized histograms are shown in Figure 8 for four different pump powers. In the limit of low collection and detection efficiency, these histograms approximate the photon correlation function [31]. The $\tau = 0$ peak shows a large reduction in area, indicating strong anti-bunching. The numbers printed above the peaks indicate the peak areas, properly normalized by dividing the histogram areas by the photon count rate at each detector, the laser repetition period, and the measurement time. For the numbers shown, the only background counts subtracted were those due to the independently determined dark count rates of the photon counters (130 s^{-1} and 180 s^{-1}), which are small compared to the total count rates (19 800 s^{-1} and 14 000 s^{-1}) for the two counters at 0.88 mW pump power. The dark counts can be subtracted because they depend only on the detectors and do not reflect any characteristics of the photon source. When counts within 2.8 ns of $\tau = 0$ were included, a normalized $g^{(2)}(\tau = 0)$ peak area of 0.12 was obtained at 0.88 mW.

An additional cause of antibunching in the experiment is suppression of the probability for the dot to absorb a second photon after a first photon has been absorbed. If one collects emission from both the single-exciton and the multi-exciton lines at a pump power of 0.44 mW, the $g^{(2)}(\tau = 0)$ peak area is still reduced to about 0.32. We believe that, once a single exciton has been created in the dot, the resonant energy for absorption is shifted, due to the electrostatic potential of the trapped carriers. This moves the absorption peak out of resonance with the exciting laser, reducing the probability of absorbing a second photon and creating a second exciton.

Note that this blockade-like mechanism does not apply for above-band excitation. In this case, as mentioned above, we expect the number of excitons created per pulse to be Poissonian. When the photon-correlation measurement was done under these conditions, the minimum area of the zero-delay peak for saturated excitonic emission was 0.3. The antibunching is then only due to the spectral selection of the single-exciton emission. If both the single-exciton and biexciton peaks were collected, the antibunching was seen to be eliminated altogether. As an additional test of the mechanism for antibunching, we tuned the pump laser 1.7 meV below the resonant wavelength for excitation of the dot, and reduced the pump power well below that required to saturate the excitonic line. This meant that the probability of absorbing a second photon should be enhanced by the absorption of a first photon, since the electrostatic energy shift will bring the absorption onto resonance with the pump laser. Indeed, we saw strong bunching under these conditions, with the zero-delay peak area being as large as 3.5. We believe that we thus have experimental support for our speculation that the suppression of multiple-photon emission is partially due to a suppressed probability of multiple-photon absorption.

The residual non-zero probability of having more than one photon per pulse is believed to be primarily due to imperfect spectral filtering. As well, there is a broadband emission background that contributes some spurious photons. By reducing the filter bandwidth, we believe another fivefold reduction in the $g^{(2)}(0)$ peak should be possible.

A similar method can be used for the generation of entangled photon pairs. Instead of filtering out only the single-exciton peak, both the exciton and the biexciton peak would be spectrally selected. The correlated electrons and holes in the biexcitonic state have opposite spins, due to the Pauli exclusion principle. This spin anticorrelation should translate into an anticorrelation in the polarization of emitted photons if the recombination follows the same selection rules as for quantum wells in direct-gap materials with a cubic lattice. In these wells, any photons emitted in the normal direction are circularly polarized, since they correspond to a $J_z = \pm 1/2$ electron recombining with a $J_z = \pm 3/2$ heavy hole [32]. This is illustrated in Figure 9, where solid arrows indicate the allowed σ^+ and σ^- transitions.

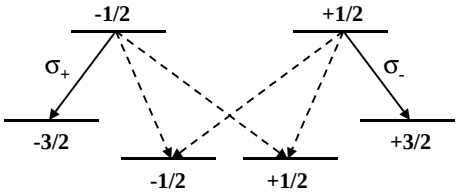

Fig. 9. Selection rules for conduction-band to valence-band transitions in a quantum well, for a crystal with cubic symmetry and a direct bandgap. The numbers above the levels are the total-angular-momentum quantum numbers. Only the transitions indicated by the solid lines will be seen in luminescence in the direction normal to the plane of the quantum well.

In the case of a quantum dot, the strong confinement introduces level mixing, and the hole ground state may have contributions from the $J_z = \pm 1/2$ hole states (or from other valence bands). Possible transitions to the $J_z = \pm 1/2$ states are indicated by dashed arrows in Figure 9. Accordingly, when a $J_z = +1/2$ electron radiatively recombines with a hole in a dot, the emitted light is predominately σ^+-polarized, but may also have a σ^- component. Thus, the two photons that arise from the decay of the biexcitonic ground state are not necessarily perfectly anti-correlated with respect to σ^+- and σ^--polarization. An asymmetric dot shape, strain, and piezoelectric effects further reduce the anti-correlation [33]. However, there is experimental evidence from polarized photoluminescence that the anti-correlation in σ^+- and σ^--polarization is preserved in quantum dots [34]. Other experiments suggest that the appropriate basis for the anti-correlation may be linear [35]; however, this does not affect our argument.

The generation of entangled photon pairs thus proceeds as follows, starting from the biexcitonic ground state of the dot. The situation is similar to a two-photon cascade decay in an atom [36]. One of the two excitons recombines first and emits a σ^+ or a σ^- photon. The second exciton, with opposite carrier spins, then recombines and emits a photon of opposite polarization. If the two decay paths are indistinguishable, the two-photon state has the same form in any linear basis and is a maximally entangled (Bell) state:

$$|\psi\rangle = \frac{1}{\sqrt{2}}(|\sigma^+\rangle_1|\sigma^-\rangle_2 + |\sigma^-\rangle_1|\sigma^+\rangle_2)\,. \qquad (5)$$

The advantage of the proposed structure compared to existing sources of entangled photons, such as two-photon cascade decay in atoms or parametric down conversion in non-linear crystals, is that entangled photon pairs are provided one by one with a high repetition rate by a compact semiconductor device.

However, certain processes may degrade the entanglement by causing an evolution of the pure state into a statistical mixture of anti-correlated photons. For example, when the quantum dot is in the biexcitonic ground state, spin dephasing may occur between the photon emission events. If the dephasing rate R_d is much larger than the radiative recombination rate γ, then the final photon state is again a statistical mixture. However, recent experiments on quantum dots indicate that the spin dephasing rate of conduction band electrons is much lower than 0.3 GHz [37], and may even be frozen out on the time scale of the radiative recombination rate [38].

4 Coupling single quantum dots to micropost microcavities

A single quantum dot is a good source of single photons and possibly of entangled photon pairs. However, the usefulness of the source for quantum communication or other applications is limited by its efficiency. Only one out of approximately every 3 000 photons emitted from the dot was ultimately detected by the single-photon detectors. The largest cause of this inefficiency is the fact that the dot emits primarily into the semiconductor substrate, and only 0.6% of the emission is collected by the aspheric lens in front of the cryostat window.

Lenses, mirrors, and other linear optical elements cannot change the brightness of a source, and are thus limited in their ability to increase the collection efficiency. However, by placing the quantum dot inside a microscopic optical cavity, its spontaneous emission characteristics can be changed, and it can be made to radiate primarily into the cavity modes. This is due to the fact that spontaneous emission is not an inherent property of the emitter, but is the result of interaction between the dipole and the surrounding electromagnetic vacuum.

The radiative transition rate of an emitter from an excited, initial state $|i\rangle$ to a lower energy, final state $|f\rangle$ depends on the available electromagnetic density of states $\rho(\lambda)$ at the transition wavelength λ. In the weak-coupling regime, where the atomic excitation is irreversibly lost to the field, this rate is expressed by Fermi's golden rule as $(2\pi/\hbar)\rho(\lambda)|\langle f|H|i\rangle|^2$, where H is the atom-field interaction Hamiltonian. Thus, by altering $\rho(\lambda)$ using an optical cavity, the spontaneous emission can be enhanced or suppressed. Looked at another way, the spontaneous emission is analogous to stimulated emission, where the "stimulating" field is not real photons, but vacuum fluctuations. By localizing the vacuum field in a resonant cavity mode, the spontaneous emission rate can be enhanced. For a localized atom with a negligible linewidth that is on resonance at the antinode of the standing wave, the enhancement factor (known as the Purcell factor) is $3Q\lambda^3/4\pi^2V_\mathrm{o}$, where Q is the cavity quality factor and V_o is the cavity mode volume. In order to couple the majority of spontaneous emission into the cavity mode, then, we require a relatively high-finesse cavity with a small mode volume.

Microscopic planar cavities can be grown by the same MBE process used to create the quantum dots. The microcavity is formed by two distributed-Bragg reflectors (DBR's) separated by a spacer layer whose thickness is equal to λ. The DBR's are dielectric mirrors consisting of alternating quarter-wavelength thick layers of AlAs and GaAs. The Fresnel reflections from the AlAs/GaAs interfaces add up in phase, resulting in high overall reflectivity within an angular and spectral stopband. There

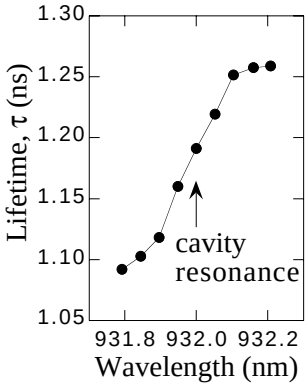

Fig. 10. Measured photoluminescence lifetime *vs.* wavelength for quantum dots in a planar microcavity.

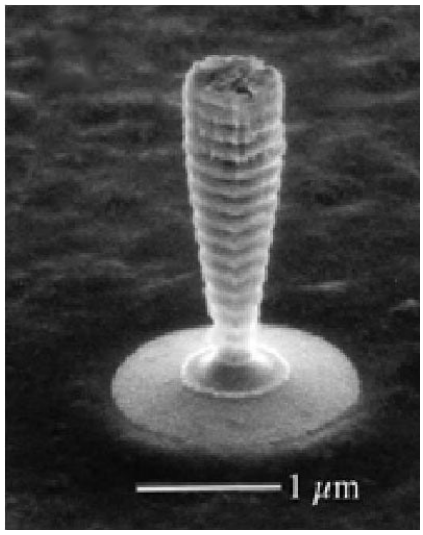

Fig. 11. Scanning-electron-microscope image of a micropost microcavity.

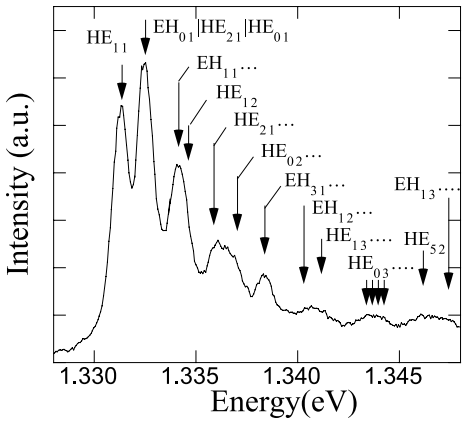

Fig. 12. Photoluminescence from a micropost microcavity with top diameter of 6 μm which contains a large number of InAs/GaAs quantum dots. Peaks correspond to different resonances of the microcavity. The arrows show calculated resonance energies, labeled according to the corresponding transverse waveguide mode.

are 29.5 mirror pairs below the spacer layer and 15 mirror pairs above. The electric field intensity has a maximum in the center of the spacer layer, where the quantum dot layer is grown.

Interaction between the planar ensemble of quantum dots and the planar microcavity allows for a limited enhancement of the spontaneous emission rate. This is similar to effects that have been seen for quantum well excitons in planar DBR microcavities [39]. Figure 10 shows the wavelength dependence of spontaneous emission lifetime for quantum dots in a planar microcavity with a resonance wavelength of 932 nm and a quality factor Q of 2 300. (See below for an explanation of the measurement technique.) Here, there is a continuous distribution of cavity modes from the resonant cut-off wavelength λ_c to a wavelength corresponding to the stopband edge. Since the number of modes increases with decreasing wavelength from the cutoff wavelength, the spontaneous emission lifetime is correspondingly decreased from 1.3 ns to 1.1 ns. In order to achieve a larger enhancement of emission rates, both the field and the exciton must be confined in all three dimensions.

Three-dimensional confinement of the field is realized at the same time as isolation of single quantum dots by etching microposts into the MBE-grown sample. Following a process similar to that described above for etching mesas, posts are etched through the top DBR mirror, through the spacer layer containing the quantum dots, and through a small portion of the lower DBR. Designed post diameters vary from 6 μm down to 0.5 μm. A scanning-electron microscope image of a post with nominal diameter of 0.5 μm is shown in Figure 11. A taper in the post diameter arises as a result of the etch, and helps reduce the cross-sectional area at the location of the quantum dots.

Due to the large index contrast between the semiconductor material and the surrounding air or vacuum, light is trapped inside the post by total internal reflection. That is, the post acts as a small waveguide for light in the transverse direction. Together with the mirrors in the longitudinal direction, this leads to three-dimensional confinement of light in the micropost microcavity. The structure exhibits discrete resonances, to which the quantum-dot emission can be efficiently coupled. This effect can be seen in the PL spectrum from dots in a 6 μm-diameter microcavity post, as shown in Figure 12. The inhomogenously-broadened quantum dot emission is filtered by the cavity modes into a series of discrete peaks. Note that we do not consider polarization in our treatment; the lowest-energy fundamental mode, for example, is actually composed of a pair of degenerate modes of opposite polarizations.

The cavity resonances can be modeled approximately following Panzarini and Andreani [40]. We assume that the electromagnetic field can be factored into a part that depend only on the transverse coordinates and a part that depends only on the longitudinal coordinate. The longitudinal field dependence is calculated by a transfer-matrix

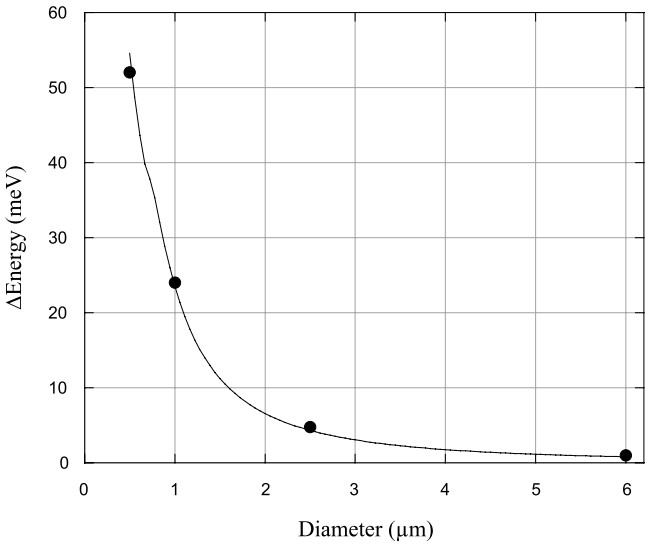

Fig. 13. Blueshift of the lowest-energy mode of micropost microcavities, as compared to the cutoff wavelength of the corresponding planar microcavity. The points are experimental data, while the solid line is the calculated result.

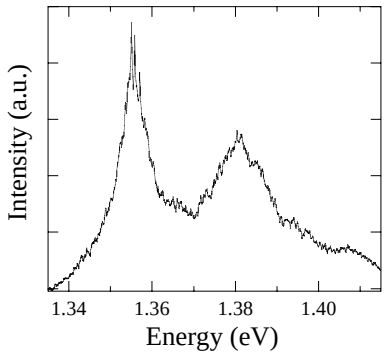

Fig. 14. Photoluminescence from a micropost microcavity with diameter of 1 μm which contains several InAs/GaAs quantum dots.

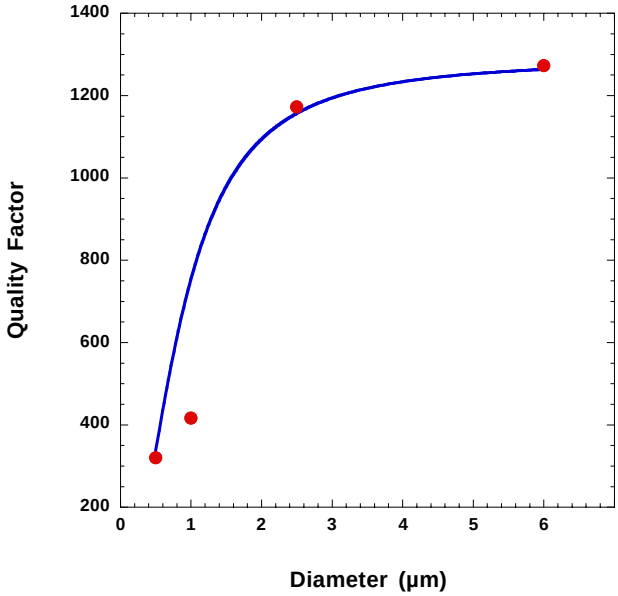

Fig. 15. Quality factor of the fundamental mode of micropost microcavities as a function of post diameter. The points are experimental data, while the solid line is the predicted result.

method, using layer thicknesses from the crystal growth, and known GaAs and AlAs refractive indices [41]. The calculated longitudinal profile gives an effective penetration depth of the cavity mode into the DBR's. In addition, an average refractive index n_{eff} is obtained by averaging over the longitudinal direction, using the field intensity as a weighting factor. The effective index is then used in a standard waveguide model to determine the transverse field dependence. Using cylindrical dielectric boundary conditions, a characteristic equation for the modal wavenumber can be solved to provide the blue shift of the cavity resonance [42]. The waveguide equations also give a transverse field dependence. By integrating the field in three dimensions, an effective mode volume is obtained.

The arrows in Figure 12 are the resonance energies calculated by this method for a post with 6 μm diameter; they are labeled according to the corresponding transverse waveguide modes. Also, Figure 13 shows agreement between measured blueshifts for the fundamental (HE_{11}) mode and blueshifts calculated by this method. Note that this agreement is obtained without any fitting parameters.

Figure 14 shows the filtered PL spectrum for a post with a top diameter of 1 μm. Comparing to Figure 12, we can see a blueshift and an increased mode spacing, due to the increased transverse confinement. However, the modal linewidth is also increased, reflecting a loss of cavity quality factor. Figure 15 shows the measured values of quality factor for different post diameters, determined from the measured PL linewidths. The degradation of Q with decreasing post diameter is believed to be primarily due to diffraction in the unetched portion of the lower DBR. The field spreads as it penetrates into the lower DBR and on its trip back to the post, and the amount of light that is recaptured by the mode is determined by the overlap of the diffracted field with the transverse mode profile of the post. A simple model of diffraction in the lower DBR is used to calculate quality factors. As can be seen in Figure 15, this model can account well for the observed loss of Q. This indicates that other loss mechanisms, such as scattering loss due to roughness of the post sidewalls, play a secondary role.

Time- and frequency-dependent emission from the quantum dots was measured using a streak camera with a spectrometer attachment, as described above. The decay at longer times is determined by a single exponential time constant, the spontaneous emission time for excitons in the quantum dot. This part of the curve was thus fitted in order to determine radiative time constants. The validity of this approach was confirmed using a detailed rate-equation model. By repeating this process at different wavelengths, the frequency-dependent emission rate across the fundamental cavity mode can be determined.

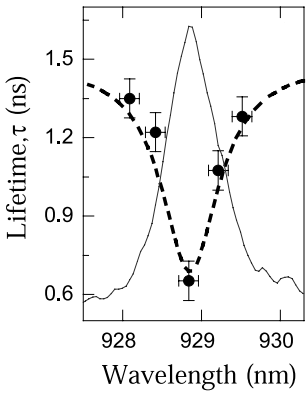

Fig. 16. Photoluminescence lifetime *vs.* wavelength for quantum dots in a micropost microcavity with a top diameter of 2 μm. The points are measured values, while the dashed line is the predicted result. The thin, solid line represents the photoluminescence intensity at the same wavelengths.

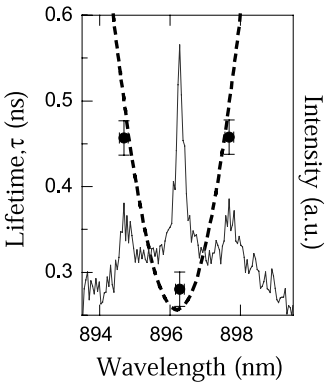

Fig. 17. Photoluminescence lifetime *vs.* wavelength for isolated quantum dots in a micropost microcavity with a top diameter of 0.5 μm. The points are measured values, while the dashed line is the predicted result. The thin, solid line represents the photoluminescence intensity at the same wavelengths.

Figure 16 shows the results for a post with 2 μm top diameter. The lifetime is a minimum on resonance with the cavity mode, a clear signature of the discrete, three-dimensional cavity resonance. As well, the lifetimes off-resonant with the mode are nearly the same as in the absence of the cavity. This indicates that the lifetime modification is due to interaction with the cavity mode, and not due to some other effect, such as non-radiative recombination.

The expected spontaneous emission rate can be calculated according to the following equation:

$$\frac{\gamma}{\gamma_0} = \frac{Q\lambda_c^3}{2\pi^2 n_{\rm eff}^3 V_0} \frac{\Delta\lambda_c^2}{\Delta\lambda_c^2 + 4(\lambda - \lambda_c)^2} + f\,, \qquad (6)$$

where γ_0 is the experimentally-determined emission rate of a quantum dot without a cavity, λ_c is the cavity resonant wavelength, $\Delta\lambda_c$ is the cavity linewidth, and $(\lambda - \lambda_c)$ is the detuning of the dot emission wavelength from the cavity resonance. The cavity quality factor and mode volume are calculated as described above. $f\gamma_0$ is the decay rate into leaky modes (*i.e.*, emission that is incident on the post edges at an angle larger than the critical angle for total internal reflection). For an ensemble of dots in the post, the calculated emission rate must be averaged radially across the post to give an expected decay rate. This rate is also plotted in Figure 16, and shows good agreement with experiment. Note again that no fitting parameters are used in the theory.

Figure 17 shows similar results for a cavity with top diameter of 0.5 μm. There is now a single quantum dot on resonance with the cavity mode. A significant reduction in the spontaneous emission time, to 0.28 ns, is seen. The dashed line is the theoretical result. This is in good agreement with the measurement, considering only diffractive losses through the bottom DBR mirror have been included in determining Q. As well, the factorization of fields into longitudinal and transverse components is inexact.

The spontaneous emission lifetime can be converted into a coupling coefficient β, the fraction of light that is captured in the fundamental cavity mode:

$$\beta = \frac{\gamma - \gamma_0 - \gamma_c}{\gamma}\,, \qquad (7)$$

where γ is the enhanced spontaneous emission decay rate into the fundamental mode of the cavity, γ_0 is the spontaneous emission decay rate in the absence of a cavity, and γ_c is the fractional spontaneous emission decay rate into the solid angle of the cavity mode in the limit that the mirror reflectivity approaches zero. Since this solid angle is at most a few degrees in our case, $\gamma_c \ll \gamma_0$. Using equation (7), we determine that 78% of the light from a single quantum dot is collected by a single mode.

Similar lifetime modifications have been reported for ensembles of quantum dots. However, systems employing large numbers of inhomogenously-broadened dots coupled to discrete optical modes may have large β and short τ values on resonance, but off-resonant β and τ values are small and long, respectively. Averaging over the ensemble of dots coupled to cavity mode, the overall β and τ values are poor. More recently, modified emission has been seen for a single quantum dot coupled to a whispering-gallery mode of a microdisk cavity [43]. However, it is difficult to efficiently couple light out of such a mode. Micropost microcavities, on the other hand, can be designed so that virtually all light escapes from the mode in a Gaussian-like wave propagating normal to the sample surface.

The coupling coefficient of 78% is limited by the relatively poor cavity quality factor for small posts. Since this is mostly due to diffraction loss in the lower DBR, the most apparent way to increase the quality factor is to etch completely through the lower mirror stack. This involves reducing the taper in the cross-section, while maintaining smooth sidewalls in order to avoid scattering loss. Although this is a fabrication challenge for sub-micron posts, we believe that it has the prospect to offer signifi-

cant improvement in Q and to give β values approaching unity.

5 Conclusions

Quantum dots can be used as sources of non-classical light. We have grown InAs/GaAs quantum dots by a self-assembly process in molecular-beam epitaxy, and have isolated single dots in microposts using electron-beam lithography and plasma etching. Spectroscopy on single dots shows an energy shift between emission from single excitons and biexcitons in the quantum dot. This means that pulsed excitation and spectral filtering can be used to isolate a single emitted photon per pump pulse. We demonstrated a tenfold reduction in the multi-photon probability as compared to attenuated coherent light. Further reduction should be possible by improved spectral filtering.

As well, we have incorporated single quantum dots into microscopic optical cavities. By modifying the spontaneous emission rate, this technique results in 78% of the light emitted from the dot being collected in a single cavity mode. The efficiency of coupling can be further improved by improving the fabrication process.

By combining these two elements, it should be possible to create an efficient source of trigerred single photons. As well, an extension of the technique should make it possible to create photon pairs that are at least partially entangled in polarization. These two sources could then be incorporated into quantum cryptography systems in order to improve the transmission rate of secure information.

We would like to thank E. Waks, J. Vuković, H. Deng, and S. Somani for valuable assistance. Financial assistance for M.P. and C.S. was provided by the Stanford Graduate Fellowship program. Financial assistance for C.S. was also provided by the National Science Foundation. Financial assistance for O.B. was provided by the Alexander von Humbolt Foundation. Financial assistance for G.S.S. was provided by the Army Research Office. This work is partially supported by U.S. Army/Research Office award number DAAD19-00-1-0172.

References

1. C.H. Bennett, G. Brassard, in *Proceedings of IEEE International Conference on Computers, Systems, and Signal Processing*, Bangalore, India (IEEE, New York, 1984), p. 175.
2. C.H. Bennett, F. Bessette, G. Brassard, L. Salvail, J. Smolin, J. Crypt. **5**, 3 (1992).
3. N. Lütkenhaus, Phys. Rev. A **61**, 2304 (2000).
4. E. Waks, A. Zeevi, Y. Yamamoto, Phys. Rev. A, to be published, e-print:`quant-ph/0012078` (Dec. 16, 2000).
5. H.J. Kimble, M. Dagenais, L. Mandel, Phys. Rev. Lett. **39**, 691 (1977); F. Diedrich, H. Walther, Phys. Rev. Lett. **58**, 203 (1987).
6. T. Basché, W.E. Moerner, M. Orrit, H. Talon, Phys. Rev. Lett. **69**, 1516 (1992); L. Fleury, J.-M. Segura, G. Zumofen, B. Hecht, U.P. Wild, Phys. Rev. Lett. **84**, 1148 (2000).
7. C. Kurtsiefer, S. Mayer, P. Zarda, H. Weinfurter, Phys. Rev. Lett. **85**, 290 (2000); R. Brouri, A. Beveratos, J.-P. Poizat, P. Grangier, Opt. Lett. **25**, 1294 (2000).
8. F. De Martini, G. Di Giuseppe, M. Marrocco, Phys. Rev. Lett. **76**, 900 (1996); B. Lounis, W.E. Moerner, Nature **407**, 491 (2000).
9. C. Brunel, B. Lounis, P. Tamarat, M. Orrit, Phys. Rev. Lett. **83**, 2722 (1999).
10. J. Kim, O. Benson, H. Kan, Y. Yamamoto, Nature **397**, 500 (1999).
11. M. Heinrich, T. Legero, A. Kuhn, G. Rempe, Phys. Rev. Lett. **85**, 4872 (2000).
12. P. Michler *et al.*, Nature **406**, 968 (2000); B. Lounis, H.A. Bechtel, D. Gerion, P. Alivisatos, W.E. Moerner, Chem. Phys. Lett. **329**, 399 (2000).
13. C. Santori, M. Pelton, G.S. Solomon, Y. Dale, Y. Yamamoto, Phys. Rev. Lett. **86**, 1502 (2001).
14. P. Michler *et al.*, Science **290**, 2282 (2000); V. Zwiller *et al.*, Appl. Phys. Lett. **78**, 2476 (2001).
15. E.M. Purcell, Phys. Rev. **69**, 681 (1946); K.H. Drexhage, in *Progress in Optics*, edited by E. Wolfe (North-Holland, Amsterdam, 1974), Vol. XII, p. 165.
16. P. Goy, J.-M. Raimond, M. Gross, S. Haroche, Phys. Rev. Lett. **50**, 1903 (1983); G. Gabrielse, H. Dehmelt, Phys. Rev. Lett. **55**, 67 (1985); R.G. Hulet, E.S. Hilfer, D. Kleppner, Phys. Rev. Lett. **55**, 2137 (1985); D.H. Heinzen, J.J. Childs, J.E. Thomas, M.S. Feld, Phys. Rev. Lett. **58**, 1320 (1987).
17. B. Ohnesorge *et al.*, Phys. Rev. B **56**, R4367 (1997); J.-M. Gérard *et al.*, Phys. Rev. Lett. **81**, 1110 (1998); L.A. Graham, D.L. Huffaker, D.G. Deppe, Appl. Phys. Lett. **74**, 2408 (1999).
18. G.S. Solomon, M. Pelton, Y. Yamamoto, Phys. Rev. Lett. **86**, 3903 (2001).
19. O. Benson, C. Santori, M. Pelton, Y. Yamamoto, Phys. Rev. Lett. **84**, 2513 (2000).
20. A.K. Ekert, Phys. Rev. Lett. **67**, 661 (1991).
21. M. Tabuchi, S. Noda, A. Sasaki, in *Science and Technology of Mesoscopic Structures* (Springer-Verlag, Tokyo, 1992), p. 375; D. Leonard *et al.*, Appl. Phys. Lett. **63**, 3203 (1993); J.-Y. Marzin *et al.*, Phys. Rev. Lett. **73**, 716 (1994); M. Grundmann *et al.*, Phys. Stat. Sol. (b) **188**, 249 (1995).
22. D. Bimberg *et al.*, *Quantum Dot Heterostructures* (John Wiley & Sons, Chichester, 1999).
23. M.A. Hreman, H. Sitter, *Molecular Beam Epitaxy: Fundamentals and Current Status*, 2nd edn. (Springer, Berlin, 1996).
24. G.S. Solomon, J.A. Trezza, J.S. Harris Jr, Appl. Phys. Lett. **66**, 991 (1995), G.S. Solomon, J.A. Trezza, J.S. Harris Jr, Appl. Phys. Lett. **66**, 3161 (1995).
25. S.A. Campbell, *The Science and Engineering of Microelectronic Fabrication* (Oxford University Press, Oxford, 1996).
26. B. Ohnesorge, M. Albrecht, J. Oshinowo, A. Forchel, Y. Arakawa, Phys. Rev. B **54**, 11532 (1996).
27. L. Landin, M.S. Miller, M.-E. Pistol, C.E. Pryor, L. Samuelson, Science **280**, 262 (1998); L. Landin *et al.*, Phys. Rev. B **60**, 16640 (1999); M. Bayer, O. Stern, P. Hawrylak, S. Fafard, A. Forchel, Nature **405**, 923 (2000).

28. J.J. Finley *et al.*, Phys. Rev. B **63**, 073307 (2001).
29. C. Santori, M. Pelton, G.S. Solomon, Y. Yamamoto, e-print:`cond-mat/0108466` (Aug. 28, 2001).
30. J.-M. Gérard, B. Gayral, J. Lightwave Technol. **17**, 2089 (1999).
31. S. Reynaud, Ann. Phys. Fr. **8**, 315 (1983).
32. C. Weisbuch, B. Winter, *Quantum Semiconductor Structures* (Academic Press, San Diego, 1991).
33. O. Stier, M. Grundmann, D. Bimberg, Phys. Rev. B **59**, 5688 (1999).
34. Y. Toda, S. Shinomori, K. Suzuki, Y. Arakawa, Phys. Rev. B **58**, R10147 (1998).
35. A. Kuther *et al.*, Phys. Rev. B **58**, R5708 (1998).
36. A. Aspect, J. Dalibard, G. Roger, Phys. Rev. Lett. **49**, 1804 (1982).
37. J.A. Gupta, D.D. Awschalom, X. Peng, A.P. Alivisatos, Phys. Rev. B **59**, R10421 (1999).
38. M. Paillard *et al.*, Phys. Rev. Lett. **86**, 1634 (2001).
39. Y. Yamamoto, S. Machida, K. Igeta, Y. Horikoshi, *Coherence and Quantum Optics*, edited by E.H. Eberly *et al.* (Plenum Press, New York, 1989), Vol. VI, p. 1249; H. Yokoyama *et al.*, Appl. Phys. Lett. **57**, 2814 (1990).
40. G. Panzarini, L.C. Andreani, Phys. Rev. B **60**, 16799 (1999).
41. G. Björk, H. Heitmann, Y. Yamamoto, Phys. Rev. A **47**, 4451 (1993).
42. A.W. Snyder, J.D. Love, *Optical Waveguide Theory* (Chapman & Hall, New York, 1983).
43. A. Kiraz *et al.*, Appl. Phys. Lett. **78**, 3932 (2001).